ANL-ART-202

Initial microstructural model for creep-fatigue damage in Grade 91 steel

---

Applied Materials Division

About Argonne National Laboratory
Argonne is a U.S. Department of Energy laboratory managed by UChicago Argonne, LLC under contract DE-AC02-06CH11357. The Laboratory's main facility is outside Chicago, at 9700 South Cass Avenue, Argonne, Illinois 60439. For information about Argonne and its pioneering science and technology programs, see www.anl.gov.

DOCUMENT AVAILABILITY

Online Access: U.S. Department of Energy (DOE) reports produced after 1991 and a growing number of pre-1991 documents are available free at OSTI.GOV (http://www.osti.gov/), a service of the U.S. Dept. of Energy's Office of Scientific and Technical Information

Reports not in digital format may be purchased by the public from the National Technical Information Service (NTIS):
U.S. Department of Commerce
National Technical Information Service
5301 Shawnee Rd
Alexandria, VA 22312
www.ntis.gov
Phone: (800) 553-NTIS (6847) or (703) 605-6000
Fax: (703) 605-6900
Email: **orders@ntis.gov**

Reports not in digital format are available to DOE and DOE contractors from the Office of Scientific and Technical Information (OSTI)
U.S. Department of Energy
Office of Scientific and Technical Information
P.O. Box 62
Oak Ridge, TN 37831-0062
www.osti.gov
Phone: (865) 576-8401
Fax: (865) 576-5728
Email: **reports@osti.gov**

Disclaimer
This report was prepared as an account of work sponsored by an agency of the United States Government. Neither the United States Government nor any agency thereof, nor UChicago Argonne, LLC, nor any of their employees or officers, makes any warranty, express or implied, or assumes any legal liability or responsibility for the accuracy, completeness, or usefulness of any information, apparatus, product, or process disclosed, or represents that its use would not infringe privately owned rights. Reference herein to any specific commercial product, process, or service by trade name, trademark, manufacturer, or otherwise, does not necessarily constitute or imply its endorsement, recommendation, or favoring by the United States Government or any agency thereof. The views and opinions of document authors expressed herein do not necessarily state or reflect those of the United States Government or any agency thereof, Argonne National Laboratory, or UChicago Argonne, LLC.

ANL-ART-202

Initial microstructural model for creep-fatigue damage in Grade 91 steel

---

Applied Materials Division
Argonne National Laboratory

September 2020

Prepared by

A. Rovinelli, Argonne National Laboratory
M. C. Messner, Argonne National Laboratory
T.-L. Sham, Argonne National Laboratory

Abstract

This report describes an initial Crystal Plasticity Finite Element Method (CPFEM) model for cyclic plasticity and damage in Grade 91 steel. The objective of this work is to develop a framework for modeling creep-fatigue interaction in Grade 91 steel to better predict the onset of damage in high temperature microreactor components. Many microreactor concepts envision low operating pressures but relatively high thermal stresses. Under these conditions, creep-fatigue will likely be the dominant design failure mechanism. Physically based models, like the one under development here, could lead to a better understanding of creep-fatigue mechanisms and the effect of stress multiaxiality and hold time on creep-fatigue damage. In turn, this could lead to more efficient microreactor component designs.

Table of Contents

List of Figures

List of Tables

1 Introduction

Uncertainty in long-term material properties and material degradation under reactor operating conditions for long service lives are the primary challenges in establishing accurate design methods for high temperature nuclear reactor structural components. The traditional approach, for example adopted by the ASME in determining the Section III, Division 5 design rules for high temperature reactor components, is to use a long-term testing database plus limited empirical extrapolation – typically a factor of three to five in time – to establish the design material properties. This is a conservative approach, as the long-term tests support the design data and the relatively short extrapolation in time limits the potential negative impact of mechanism shifts or other unexpected material behavior.

The current qualification process has two main shortcomings:

1. Long-term testing requirements limit the time between the development of a new material and its qualification for use.

2. There are some aspects of material behavior that either cannot be or are not commonly directly tested. The qualification process relies on shorter-term tests or reasonable assumptions in fixing these ancillary material properties.

Examples of these ancillary properties include the effect of multiaxial stress on creep rupture and creep fatigue damage in the material. Long-term multiaxial creep-fatigue test data is not available and so the design method makes reasonable assumptions based on limited short term testing and multiaxial creep rupture tests.

Physically-based models are one way to reduce the long-term testing requirements and improve the accuracy and efficiency of high temperature design methods. Unlike empirical extrapolation techniques, physically-based models relate the material behavior to underlying, physical, microstructural mechanisms. These models typically extrapolate with better accuracy away from the experimental database – for example to longer service lives or from uniaxial to multiaxial loading conditions. The extreme example of a physically-based model is an ab initio model, where the model begins with first principle, atomistic physics. These models readily transfer to any loading conditions because the basic laws of physics are invariant with respect to time, loading direction, and so on. Complete ab initio models for relevant high temperature structural properties are not available. However, physically-based models that incorporate the critical microstructural features, deformation mechanisms, and damage mechanisms, even when partly calibrated to experimental data, make more accurate predictions outside the experimental database than purely empirical models.

This report describes the initial development of a microstructural model for creep-fatigue in Grade 91 steel. Grade 91 is a ferritic-martensitic alloy with excellent high temperature properties up to about 600° C. It is currently slated for use in future high temperature, heat-pipe cooled, core block microreactors.

This report describes the groundwork needed to extend a physically-based model for monotonic creep deformation and damage in Grade 91 steel to creep-fatigue deformation. The previous monotonic model developed at Argonne National Laboratory (ANL) was successful in predicting [1–4]:

1. Long-term uniaxial creep curves and associated rupture lives

2. An experimentally-observed shift in the creep rate stress sensitivity, attributed through the model to a mechanism shift between dislocation and diffusion-dominated creep.
3. A new effective stress measure that captures simulated multiaxial rupture data better than the current ASME effective stress measure for Grade 91.
4. A switch from a notch-strengthening to a notch weakening behavior as a function of the applied stress/ rupture life.

All of these key observations could be factored into the ASME high temperature design method. The new effective stress, in particular, is likely to immediately affect the design Code through incorporation in a nuclear code case providing a new steady state, primary load design method [5].

A physically-based model for creep-fatigue could provide similar design information for Grade 91. The model could be used to examine, in particular, the Code assumptions for:

1. How creep-fatigue occurs in components undergoing actual service loads, which tend to have lower primary and secondary stress magnitudes than accelerated, relatively short-term creep-fatigue testing.
2. How the Code's assumptions for multiaxial creep-fatigue compare to realistic, physically based simulations. Experimental multiaxial creep-fatigue test data is essentially unavailable.

The second issue is particularly important for core block microreactors where the core block itself has a complicated geometry and does not resemble the biaxial vessel structures considered by the original developers of the ASME high temperature design method. Moreover, preliminary analysis of core block reactor-type components suggests that the secondary, thermal stresses will heavily constrain the design and so creep-fatigue will control the maximum permissible component life. A better understanding of multiaxial creep-fatigue in the relevant materials will be needed to design more efficient core block components.

There has been comparatively little microstructural modeling and simulation work on creep-fatigue damage. Experimentally, creep-fatigue interaction is the observation that a strain-controlled cyclic test will have a shorter number of cycles to failure if holds at constant strain are included on either one or both ends of the strain cycle when compared to a corresponding test at the same conditions without a hold. There is no general agreement on the mechanism causing creep-fatigue interaction. There are two general schools of thought:

1. Creep damage occurs first and initiates or accelerates the growth of microcracks through fatigue [6].
2. Cracks initiate through fatigue mechanisms and material softening, either through creep void cavitation or thermal softening mechanisms, accelerates the growth of these fatigue cracks [7, 8].

The first school is then "fatigue damage enhances creep crack growth" and the second school is "creep enhances fatigue crack growth." There may be no general mechanism for creep-fatigue interaction, it may be material-dependent [9, 10]. One reason to develop a microstructural model for creep-fatigue interaction is to better understand the underlying material mechanism.

Microscale modeling approaches have thus far been limited to either just low cycle fatigue (c.f. [11]) or just monotonic creep (c.f. [12]). Integrating the two mechanisms into a single model, for example in a crystal plasticity finite element (CPFE) framework, poses substantial modeling and numerical challenges. A model must:

1. Represent creep damage through grain boundary (GB) cavity nucleation and growth. This damage model must be robust and handle cyclic deformation with the associated unloading and grain boundary contact.

2. Accurately capture the details of creep and cyclic plasticity in the grain bulk, including kinematic hardening and creep-plasticity interactions.

3. Model the development of trans-granular fatigue cracks, following their development from, at least, nucleation to fully-developed microcracks.

4. Remain numerically stable for many cycles of reverse loading.

5. Be numerically efficient in order to simulate large numbers of load cycles in a reasonable amount of time.

This report describes a preliminary model for creep-fatigue in Grade 91 covering items 1, 2, and, to a lesser extent, 4 and 5. Implementing a fatigue damage mechanism in the ANL CPFEM framework is future work, described in Chapter 4.

Chapter 2 describes significant improvements to the ANL model for GB creep damage. These improvements were required to develop a model that provides stable, accurate GB cavitation predictions for models subjected to cyclic load. This included significant work on models for contact between two cracked grain boundaries, for example on the compressive leg of a cyclic test for a simulation cell that has been partially damaged. Chapter 3 then describes modifications to the ANL crystal model representing grain bulk deformation in the CPFEM model aimed at capturing the details of cyclic plasticity in Grade 91. These modifications added configurable kinematic hardening to the original model, which was suitable only for monotonic deformation. Finally, Chapter 4 summarizes the work and describes the remaining work required to complete the final creep-fatigue model, notably the integration of fatigue damage into the CPFEM framework.

2 Improvements to the grain boundary cavitation model to capture creep-fatigue behavior

Creep-fatigue experiments are performed at a fixed temperature, under strain controlled loading conditions. A creep-fatigue cycle is characterized by a maximum strain, ε_{max}, a minimum strain, ε_{min}, a hold time at maximum strain, $H_{\varepsilon_{max}}$, and a hold time at minimum strain, $H_{\varepsilon_{min}}$. Figure 2.1 is a schematic representation of a general creep-fatigue cycle.

Therefore, to capture the creep-fatigue behavior of a material, the micro-mechanical model used to describe the GB cavitation process must be numerically stable under a wide range of loading conditions, including under prolonged compressive stress (for example in a compression hold). Furthermore, during a creep-fatigue experiment not all grain boundaries fail at the same time. After a grain boundary fails the two grains might come into contact when load is reversed. Modeling this contact is important, as it can be a load-carrying mechanism during compression. Furthermore, creep and creep fatigue are characterized by large area changes. Large area changes influence the traction value at the grain boundary and therefore, the cavitation process. Hence, including interface area changes is important to correctly predict the creep and creep-fatigue life of a specimen. This chapter describes improvements to the grain-boundary cavitation model to meet these requirements.

2.1 Grain boundary cavitation model rate Equation

The grain boundary cavitation model rate equations utilized in this work are the ones proposed in [4]. The grain boundary cavitation model considers five variables: the average cavity half-radius a, the number of cavities per unit area N, the normal traction T_N, and the two shear traction T_{S_1} and T_{S_2}. The number of cavities per unit area is geometrically related to the average cavity half-spacing b by:

$$b = \frac{1}{\sqrt{\pi N}} \tag{2.1}$$

The rate equation associated to the evolution of the each state variables are:

$$\dot{a} = \frac{\dot{V}}{4\pi h(\Psi) a^2} \tag{2.2}$$

$$\dot{b} = -\pi b^3 F_N \left(\frac{\langle T_N \rangle}{\Sigma_0}\right)^{\gamma} \dot{\varepsilon}^C_{eq} \quad \text{active if} \quad \left(\frac{\langle T_N \rangle}{\Sigma_0}\right)^{\beta} \int_0^T |\dot{\varepsilon}^C_{eq}| dt \geq \frac{N_I}{F_N} \quad \text{once} \tag{2.3}$$

$$\dot{T}_N = \left([\![\dot{u}]\!]_N + \frac{\dot{V}\,(T_N)}{\pi b^2} \right) C_N \tag{2.4}$$

$$\dot{T}_{S_1} = \left([\![\dot{u}]\!]_{S_1} + \frac{T_{S_1}}{\eta_S f_S} \right) C_S \tag{2.5}$$

$$\dot{T}_{S_2} = \left([\![\dot{u}]\!]_{S_2} + \frac{T_{S_2}}{\eta_S f_S} \right) C_S \tag{2.6}$$

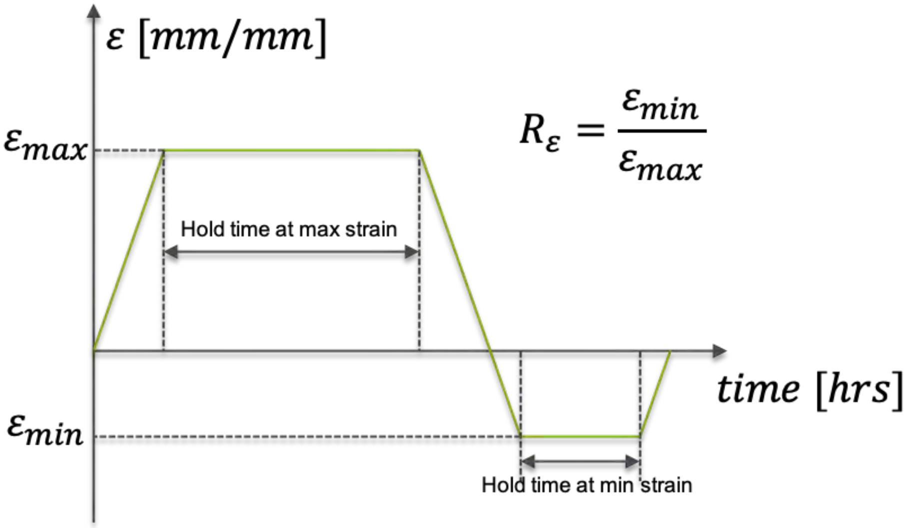

Figure 2.1: Schematic representing a general creep-fatigue cycle.

where, β, n, a_0, b_0, D, ψ, Σ_0, $\frac{F_N}{N_I}$, $\frac{N_max}{N_I}$ are model parameters (see Table 2.1 for more details), $\dot{V}$ represents the cavity volume rate (see Eq. 2.10), C_N and C_S are the interface normal and transverse elastic stiffness (Eq. 2.7 and Eq. 2.8), and f_s is function describing the change of the grain boundary sliding viscosity with damage (Eq. 2.9). In these and subsequent expressions $\langle\rangle$ are the Macaulay brackets.

$$C_N = \frac{W}{E_{GB} E_{penalty}\left(\llbracket u \rrbracket_N\right)\left(1 - \frac{a}{b}\right)} \tag{2.7}$$

$$C_S = \frac{W}{G_{GB}\left(1 - \frac{a}{b}\right)} \tag{2.8}$$

$$f_S = \begin{cases} 1 \quad \text{if} \quad \frac{a}{b} =< 0.5 \\ 2\left(-\frac{a}{b} + 1\right) \quad \text{if} \quad \frac{a}{b} =\geq 0.5 \end{cases} \tag{2.9}$$

In Equation 2.7 $E_{penalty}\left(\llbracket u \rrbracket_N\right)$ is the interpenetration penalty factor, which is a function of the normal displacement jump. Subsection 2.4.1 describes the quadratic formulation of the interpenetration penalty factor adopted here. The parameter $P|_{-W} = 10$ used in the $E_{penalty}\left(\llbracket u \rrbracket_N\right)$ factor, has been selected to recover the same interpenetration penalty used in [4].

$$\left\{\begin{aligned}
&\dot{V} = \dot{V}^D + \dot{V}^{triax}\\
&\dot{V}^D = 8\pi D\frac{T_N}{q\left(f\right)}\\
&\dot{V}^{triax} = \begin{cases} 2\dot{\varepsilon}^C_{eq}a^3\pi h(\Psi)m\left\{\alpha_n|\dfrac{\sigma_H}{\sigma_{VM}}| + \beta_n(m)\right\}^n & \text{if} \quad |\dfrac{\sigma_H}{\sigma_{VM}}| \geq 1\\ 2\dot{\varepsilon}^C_{eq}a^3\pi h(\Psi)\left\{\alpha_n + \beta_n(m)\right\}^n\dfrac{\sigma_H}{\sigma_{VM}} & \text{if} \quad |\dfrac{\sigma_H}{\sigma_{VM}}| < 1 \\ & \end{cases}\\
&\text{with}\left\{\begin{aligned}
&f = \max\left(\frac{a^2}{\left(a+1.5L\right)^2}, \frac{a^2}{b^2}\right), \quad L = \left(\frac{D\sigma_{VM}}{\dot{\varepsilon}^C_{eq}}\right)^{\frac{1}{3}}\\
&q\left(f\right) = 2\log\left(\frac{1}{f}\right) - \left(1-f\right)\left(3-f\right)\\
&h\left(\Psi\right) = \left(\frac{1}{1-cos\left(\Psi\right)} - \frac{cos\left(\Psi\right)}{2}\right)\frac{1}{sin\left(\Psi\right)}\\
&m = sign\left(\sigma_H\right)\\
&\beta\left(m\right) = \frac{\left(n-1\right)\left[n+g\left(m\right)\right]}{n^2}\\
&g\left(m\right) = \begin{cases} \log\left(3\right) - \dfrac{2}{3} & \text{if} \quad m = 1\\ \dfrac{2\pi}{9\sqrt{3}} & \text{if} \quad m = -1\\ 0 & \text{if} \quad m = 0 \end{cases}\\
&\alpha_n = \frac{3}{2n}
\end{aligned}\right.
\end{aligned}\right. \tag{2.10}$$

Equations 2.2 thorough 2.10 define a system of ordinary differential equation that must be solved simultaneously. The rate equations describing the evolution of the nonlinear state variables (e.g. Eqs. 2.2-2.6) are integrated numerically utilizing a backward Euler integration scheme:

$$x_i^{t+1}\left(x_i^{t+1}\right) = x_i^t + \Delta t\dot{x}\left(x_i^{t+1}\right) \tag{2.11}$$

where the index i refers to one of the rate variables, and the index t refers to the finite element step. The nonlinear system resulting from the backward Euler integration scheme is solved utilizing a classic Newton-Raphson method solving for the integrated variables x_i. The residual of each state variable is:

$$R_i = x_{guess,i} - x_i^{t+1}\left(x_{guess,i}\right) \tag{2.12}$$

where x_i^{t+1} is obtained using Eq. 2.11. A noticeable improvement compared to the previous implementation is including the shear traction in the nonlinear systems of equations. Coupling the shear traction in the nonlinear system guarantees more accurate results during loading, unloading, and hold in a creep-fatigue cycle.

symbol	description	value	units
β	traction nucleation exponent	2	unitless
n	creep rate exponent	5	unitless
a_0	initial cavities half radius	$5 \cdot 10^{-5}$	mm^2
b_0	initial cavities half spacing	0.06	mm^2
D	grain boundary diffusion coefficient	$1 \cdot 10^{-15}$	$^{mm^3}/_{\mathrm{MPa} \cdot \mathrm{h}}$
Ψ	cavity half tip angle	75	$\circ$
Σ_0	traction normalization parameter	200	MPa
$\frac{F_N}{N_I}$	normalized nucleation rate constant	$2 \cdot 10^4$	$^1/_{mm^2}$
$\frac{N_{max}}{N_I}$	normalized maximum cavity density	$1 \cdot 10^3$	unitless
E_{GB}	interface Young modulus	$150 \cdot 10^3$	MPa
G_{GB}	interface in-plane Shear modulus	$58.63 \cdot 10^3$	MPa
η_S	sliding viscosity	$1 \cdot 10^6$	$^{MPa \cdot h}/_{mm}$
W	interface thickness	0.011	mm
$P\|_{-W}$	penalty at $[\![u]\!]_N =$ -W	10	unitless

Table 2.1: Grain boundary cavitation material parameters.

2.1.1 Consistent substep tangent

The convergence rate of the finite element solver partly dictates the computational cost of a CPFEM simulation. For a classical nonlinear solver, such as the Newton-Raphson method, the convergence rate is strictly related to the quality of the Jacobian matrix. If the Jacobian matrix is exact then the Newton-Raphson method can achieve quadratic convergence. Quadratic convergence is key to reduce the computational cost, as it means the total simulation will require fewer nonlinear iterations and, critically, fewer linear system solves. The cost of solving the global linear system of equations in an implicit finite element method often dominates the cost of the rest of the numerical simulation, including the stress update.

Another factor influencing the computational cost is the ability of the material point nonlinear solver to converge given the parameters provided to it from the finite element solver. Even if a single material point is not able to solve the material constitutive equations then a global increment cutback is required. When a global cutback is performed all the computational time spent for current increment is wasted. Adaptive substepping at the material point level can then significantly reduce the overall cost of a simulation. While adaptive substepping was already implemented in the previous fiscal year model, the algorithmic tangent consider the substep algorithm, E, was not exact. For a traction separation law, the algorithmic tangent is defined as the total derivative of the traction w.r.t. the displacement jump:

$$E = \frac{dT}{d[\![u]\!]} = \frac{dT}{d\Delta T}\frac{d\Delta T}{d\Delta[\![u]\!]}\frac{d\Delta[\![u]\!]}{d[\![u]\!]} = \frac{d\Delta T}{d\Delta[\![u]\!]} \tag{2.13}$$

The exact algorithmic tangent is required at every Gauss point in order to achieve quadratic convergence of the global finite element solver. Adaptive substepping together with an exact algorithmitic tangent greatly reduces the overall simulation computational cost. This is especially significant for creep-fatigue loading conditions because damage is mostly accumulated during the hold, while most of the computational time is spent solving transients. The consistent algorithmic tangent for a single step can be computed using the implicit function theorem. The implicit function theorem states that if a function $F(x, y)$ is continuously differentiable w.r.t. x and y, than in the neighborhood of a root x_0, y_0 the following equation holds:

$$\frac{\partial F}{\partial x} + \frac{\partial F}{\partial y}\frac{dx}{dy} = 0 \tag{2.14}$$

Using Eq. 2.14:

$$\frac{dx}{dy} = -\left[\frac{\partial F}{\partial y}\right]^{-1}\frac{\partial F}{\partial x} \tag{2.15}$$

where $\frac{dx}{dy}$ is the consistent tangent. When solving a nonlinear system of equations the function F is the residual R, x is the vector of unknowns and y represents equation parameters, $\frac{\partial F}{\partial x}$ is the Jacobian of the nonlinear system, and $\frac{\partial F}{\partial y}$ are the partial derivatives of the residual equations w.r.t to the parameters. Notice that when solving at a material point for the traction T, the displacement jump vector $[\![u]\!]$ is considered a parameter, because it is provided by the finite element framework. When applying adaptive substepping to a traction separation law at a material point, the total displacement jump increment is subdivided in multiple subincrements:

$$\Delta[\![u]\!] = \sum_{n=1}^{N} \alpha_n \Delta[\![u]\!] \quad \text{subject to} \quad \sum_{n=1}^{N} \alpha_n = 1 \tag{2.16}$$

where N is the total number of subincrements, n is the subincrement index and α_n is the subincrement fraction. Subincremnt fractions are not required to be equal. For an adaptive substepping scheme of this type Perez-Foguet et al. [13] demonstrated that the consistent tangent E can be computed using the following recursive formula:

$$E_{n+1} = J_{n+1}^{-1}\left(-\alpha_{n+1}\left.\frac{d\Delta T}{d\Delta[\![u]\!]}\right|_{n+1} + E_i\right) \tag{2.17}$$

Equation 2.17 has been implemented in the material solver responsible for calculating the solution of the grain boundary cavitation model, providing an exact algorithmic tangent to the finite element solver for load increments requiring adaptive substepping.

2.2 Augmented grain boundary cavitation model

The new implementation uses Lagrange multipliers to enforce physical constraints on the state variables of the grain boundary cavitation model. These physical constraints arise from the following assumptions. We assume that cavities nucleate at grain boundaries because of carbide decohesion. Decohesion happens because of vacancies accumulating around carbides. When enough cavities are present the interface between a carbide and the surrounding grains vanishes, leaving a void. Nucleation is a damaging event. Once a void nucleates it cannot be healed. Therefore the number of nucleated cavities per unit area, N, can remain stationary or increase, but it cannot decrease, thus resulting in the following constraint:

$$N_{t+1} \geq N_t \quad \forall t \tag{2.18}$$

where t is an index referring to time. Recalling that the average cavity half spacing, b, is related to N by equation 2.1, the above constraint can be reformulated as:

$$b_t \geq b_{t+1} \quad \forall t \tag{2.19}$$

Once a void nucleates, it will expand or shrink depending on the loading conditions. However, because the carbide is still present inside the void, the minimum void radius will be bounded by the carbide size. Therefore the void radius a must be always grater or equal than the initial carbide size a_0:

$$a \geq a_0 \tag{2.20}$$

When the average cavity radius is equal to the cavity half spacing the grain boundary is fully damaged. Such physical constraint is not explicitly embedded in the grain boundary cavitation rate equations, therefore the nonlinear solver might converge to a solution that is numerically acceptable but physically incorrect. This potential issue is avoided including the following constraint equation:

$$b \geq a. \tag{2.21}$$

Constraints 2.19, 2.20 and 2.21 are added to the grain boundary cavitation model using three Lagrange multipliers, one for each constraint. Adding a constraint using the Lagrange multiplier methodology augments the nonlinear system by adding an additional nonlinear variable (e.g. the Lagrange multiplier λ). The Lagrange multiplier contributes to the residual of the constrained equations, and requires the introduction of an additional equation. Both the residual contribution and the additional equations are functions of the constraint equation g. The three constraint equations resulting from 2.19, 2.20 and 2.21 are:

$$g_1 \quad a - a_0 \geq 0 \tag{2.22}$$

$$g_2 \quad b_t - b_{t+1} \geq 0 \tag{2.23}$$

$$g_3 \quad b - a \geq 0 \tag{2.24}$$

The residual contribution of each constraint g_i to the state variable x_j is:

$$R_{j,i} = \lambda_i \frac{\partial g_i}{\partial x_j} \tag{2.25}$$

where λ_i is the Lagrange multiplier associated to constraint i. Lagrange multiplier are additional variables and each Lagrange multiplier is associated to a residual equation. The additional residual equation associated with each Lagrange multiplier i is:

$$R_i = \max\left(-\lambda_i, g_i\right). \tag{2.26}$$

All the results presented in this work utilize the augmented grain boundary cavitation model.

2.3 Large deformation cohesive zone model

For creep-ductile materials failure occurs after a large cross-sectional area reduction. The area reduction factor at rupture, $R_A = 1 - \frac{A_{rupture}}{A_0}$, can reach values larger than 80%. Therefore, large area changes and interface rotations need to be accounted for in the interface cohesive formulation.

The large deformation cohesive zone model has been developed for MOOSE as an extension to the base discontinuous Galerkin cohesive zone model we developed in the previous years [3, 4].

The large deformation model utilizes a total Lagrangian formulation and imposes equilibrium on the undeformed configurations using the first Piola-Kirchoff traction, T_{PK1}. The first Piola-Kirchoff traction is defined as the traction resulting from the infinitesimal force , df, acting on the undeformed area. The large deformation model assumes constitutive equations to be defined in the deformed configuration and to return the the true traction T. The true traction and the first Piola-Kirchoff traction are related to each other by the following equation:

$$df = T_{PK1} dA_0 = T dA \tag{2.27}$$

where dA_0 and dA are the deformed and undeformed infinitesimal cohesive areas. The cohesive area always refers to the interface mid-plane area. However, the interface model implementation in MOOSE does not maintain a material point on the midplane. Therefore, the interface deformation gradient F has been defined as the average of the deformation gradient on the two initially coincident surfaces:

$$F = \frac{F^+ + F^-}{2} \tag{2.28}$$

where the superscripts $+$ and $-$ identify the primary and secondary cohesive surfaces.

To test the augmented grain boundary cavitation model's ability to correctly capture large area changes and accommodate large compressive stresses we performed a simple test simulation. The simulation includes two grains and is performed under stress controlled boundary conditions. First a positive nominal traction of 100 MPa is imposed on the top surface, held for 100 h, and then a negative nominal traction of -500 MPa is imposed. Figure 2.2 is a rendering of the simulation at different times, showing large interface area changes under compression. Figure 2.3 compares the applied nominal traction versus the Cauchy interface traction. The true interface traction reduces while the interface area increases because of grain's plastic deformation. Figure 2.4 depicts the evolution of the cavity half radius and of the half cavity spacing. Notice how nucleation is inhibited during compression and how the cavity radius does not decrease below the imposed minimum value $a_0 = 5e-5$ mm.

2.4 Failure and soft contact model

The damage D in the grain boundary cavitation model is the ratio between the cavity half radius and cavity half spacing:

$$D = \frac{a}{b} \tag{2.29}$$

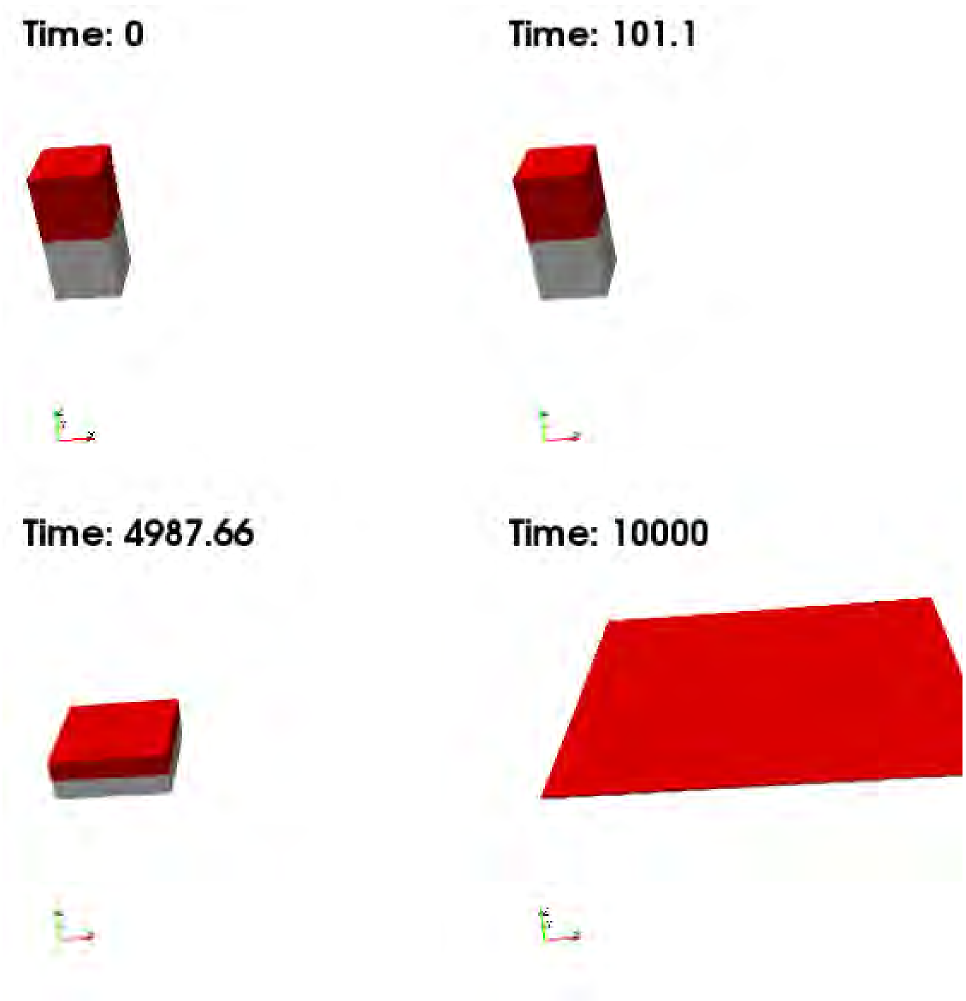

Figure 2.2: Two grains, tension-compression simulation rendering.

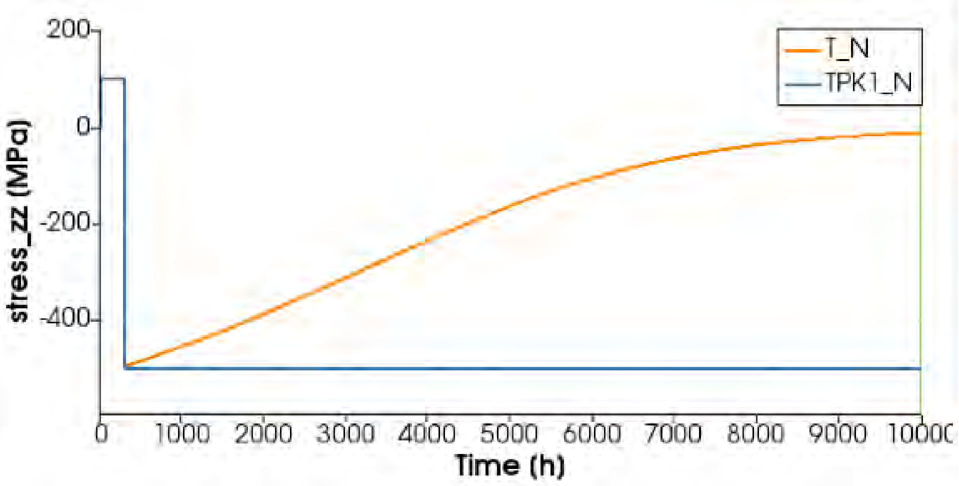

Figure 2.3: Comparison of the applied nominal normal traction $T_{N,PK1}$ and the calculated interface Cauchy traction T_N.

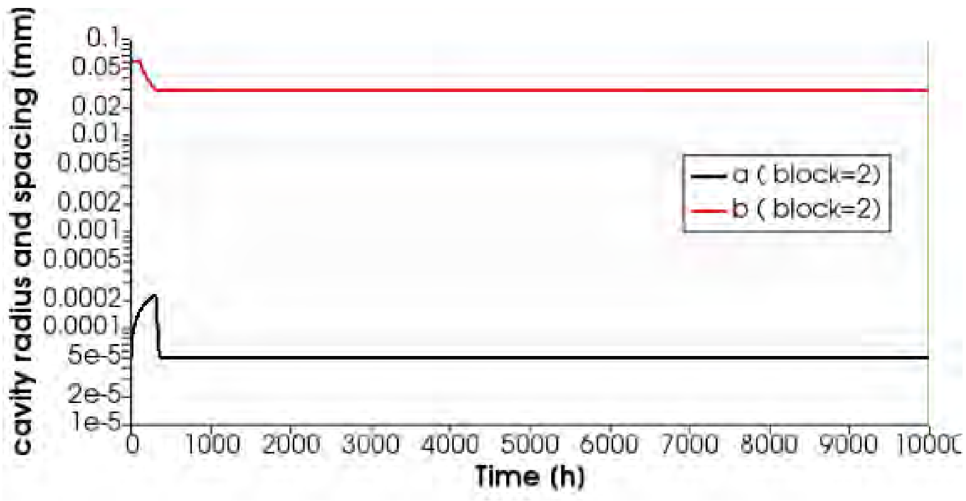

Figure 2.4: Evolution of the cavity half radius, a, and cavity half spacing, b, under compression.

Ideally the model would retain the grain boundary cavitation model until $D = 1$. However, damage accumulation follows an exponential law and thus generates extremely rapid changes in the grain boundary stiffness. Solving for such rapid stiffness changes requires very small global timesteps. To avoid an unnecessary reduction of the global time-step, the interface model switches to a simpler and more stable traction separation law when an interface integration point is close to failure. A point can be close to failure if its expected residual life is short, if its damage is close to 1, or if an unreasonably high normal traction is detected. The expected residual life is estimated using the most recent damage and damage rate, $\dot{D}$, and it is calculated by linearly extrapolating the time required to reach a damage value of 1:

$$rl = \frac{1 - D}{\dot{D}} \tag{2.30}$$

To determine if an interface integration is close to failure, we use three parameters: a maximum critical damage D_{cr}, a minimum critical residual life, rl_{cr}, and a maximum critical traction $T_{N,cr}$.

1. The damage $D \geq D_{cr}$
2. The projected residual life $rl \leq rl_{cr}$
3. The maximum critical traction $T_N \geq T_{N,cr}$

All the critical quantities are model parameters and are the same for all interface material points. When using the adaptive substepping the conditions are checked for every substep. When failure is detected during substepping the remaining portion of the total increment utilizes the failure model. When any of the failure conditions is satisfied at an integration point the integration point is marked as failed and the following quantiles are recorded:

1. The time at failure t_{fail}

2. The residual life at failure rl_{fail}

3. The displacement jump at failure $[\![u]\!]_{fail}$

4. The traction at failure T_{fail}

When an interface integration point is marked as failed the failure model takes over. The failure model is an elastic spring with an initial length and preload (e.g. $F = K(t)(x - x_0(t)) + F_0(t)$) where the spring stiffness, K and the preload F_0 both decay with time at the same rate. The exponentially decaying preload F_0 is the traction at failure multiplied by an exponential decay factor DF. The exponentially decaying stiffness of the spring is the interface elastic stiffness at failure multiplied by the same decay factor DF. The elastic stiffness at failure is computed as the ratio between the traction at failure and the displacement jump at failure. This model is describe by Eqs. 2.31 through 2.33.

$$T_i = \left([\![u]\!]_i - [\![u]\!]_{i,fail} DF\right) C_i + T_{i,fail} DF \tag{2.31}$$

$$C_i = \begin{cases} \max\left(\left|\frac{T_{i,fail}}{[\![u]\!]_{i,fail}}\right| DF, C_{min}\right) E_{penalty} & \text{if } i = 1 \\ \max\left(\left|\frac{T_{i,fail}}{[\![u]\!]_{i,fail}}\right| DF, C_{min}\right) & \text{if } i > 1 \end{cases} \tag{2.32}$$

$$DF = \exp\left(-\frac{t - t_{fail}}{0.5 rl_{fail}}\right) \tag{2.33}$$

where i is an index ranging from 1 to 3 and referring to the interface natural coordinate system. $i = 1$ refers to the normal direction while $i = 2$ and $i = 3$ refer to the two arbitrary interface tangential directions.

There are two noticeable improvement compared to the previous, monotonic model:

1. The exponential decay of the spring initial length (Eq. 2.31). This change restores a zero traction condition for $[\![u]\!]_i = 0$.

2. The introduction of the $E_{penalty}$ factor in Eq. 2.32 representing a contact response when interpenetration occurs after failure $[\![u]\!]_1 < 0$.

Correctly capturing interpenetration and contact is critical in capturing the response of failed interfaces coming into contact because of the applied boundary conditions. Neglecting the contact effect would result in overloading the unfailed grain boundaries, resulting in incorrect creep-fatigue life predictions. A further modification, a quadratic penalty formulation described in Section 2.4.1, keeps the contact response numerically stable.

Table 2.2 describes the failure model parameters.

The soft contact model has been tested on a simple domain including two grains and a single grain boundary with remote stress boundary conditions. Stress controlled boundary conditions have been used for testing because they are more prone to cause numerical oscillations. The test case works as follows: first positive a traction is applied until the grain

symbol	description	value	units
$W_{failure}$	interface thickness of the failure model	0.011	mm
$P\|_{W_{failure}}$	penalty at $[\![u]\!]_N = -W_{failure}$	1e8	untiless
rl_{cr}	minimum allowed residual life	10	h
D_{cr}	critical damage	0.95	untiless
$T_{N,cr}$	maximum allowed traction	1.4e4	MPa

Table 2.2: Failure model parameters.

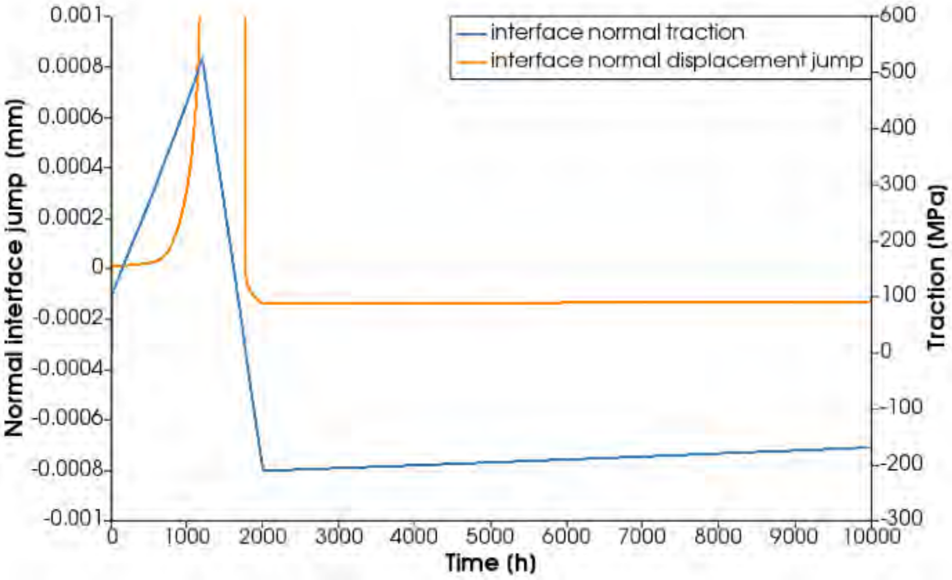

Figure 2.5: Results of a stress controlled simulation where the soft contact model is used to prevent interpenetration. The interface displacement jump is plotted on the left axis, while the interface traction is plotted on the right axis. Contact happens at $t \approx 1800$.

boundary fails ($t \approx 1200$). After failure happens a negative traction is imposed. At time $t \approx 1800$, the two grains come into contact, e.g. $[\![u]\!]_N < 0$ and the soft contact starts providing a traction to prevent interpenetration. Figure 2.5 depicts the real interface traction and the interface displacement jump against simulation time. With soft contact some interpenetration happens before the interface traction is able to counterbalance the imposed normal stress. However after some time interpenetration becomes stationary and the grains start deforming again. This is the expected behavior. Figure 2.6 is a rendering of the simulation at different times, showing that the soft contact model is able to prevent excessive interpenetration. The model parameters control the amount of interpenetration, though there is a tradeoff between numerical stability and the amount of interpenetration.

2.4.1 Continuous interpenetration penalty formulation

For elements that haven't failed yet, interpenetration is avoided by artificially increasing the effective interface stiffness, K_{eff}, using a penalty function, P , when element interpenetration

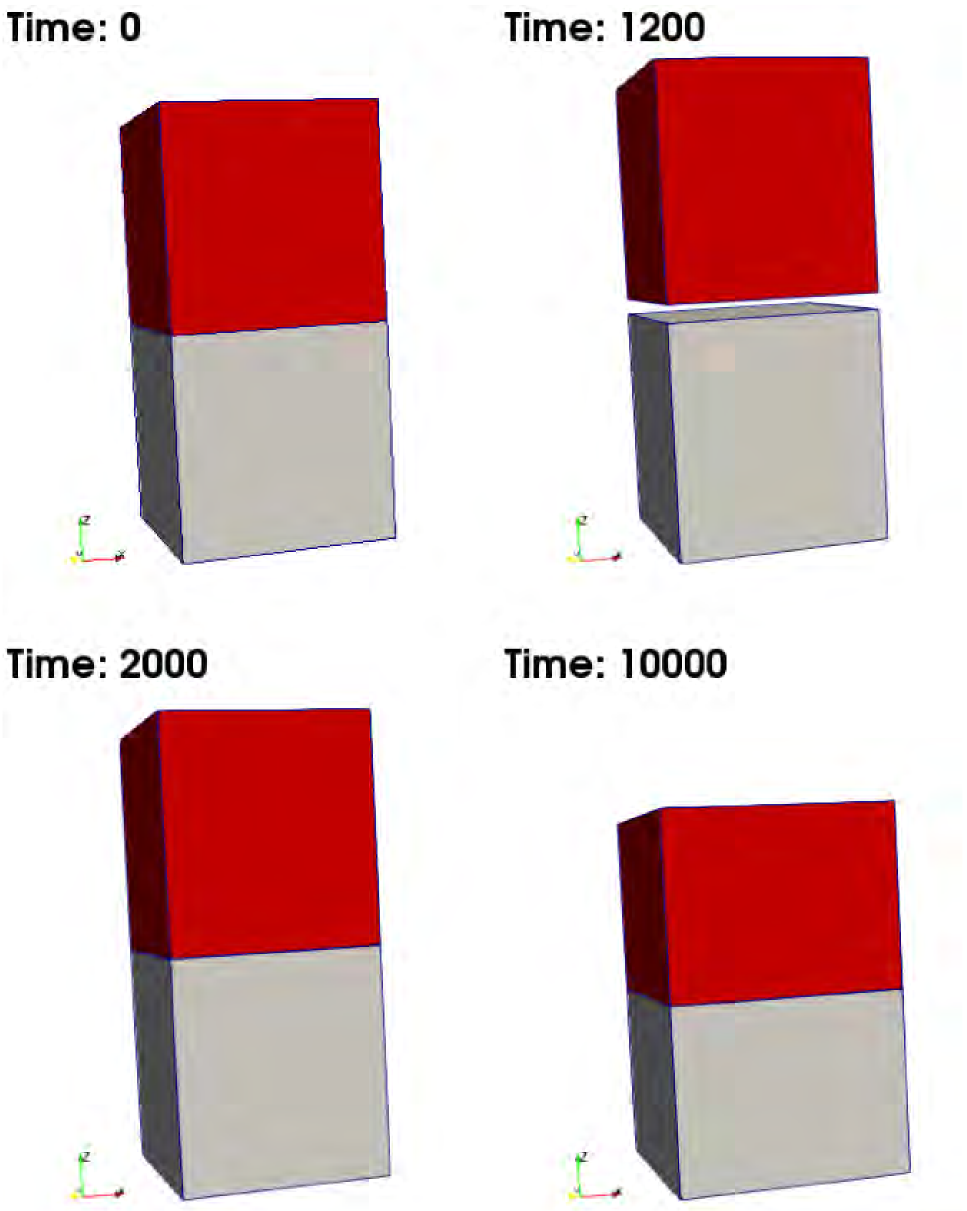

Figure 2.6: Render view of the soft contact simulation at different points in time. Top-left, simulation begins, top-right a few instants before the grain boundary fails, bottom-left after contact happens, bottom-right end of simulations. After the model establishes soft contract grain deformation resumes.

is detected

$$C_{eff} = C_{interface} P. \tag{2.34}$$

The simplest approach is to utilize a discontinuous penalty function for which a penalty P^* is used when the normal displacement jump $[\![u]\!]_\perp$, becomes smaller than a given value $[\![u]\!]_\perp^*$:

$$P = \begin{cases} 1 \quad \text{if} \quad [\![u]\!]_\perp \geq 0 \\ \\ P^* \quad \text{if} \quad [\![u]\!]_\perp < [\![u]\!]_\perp^* \end{cases} \tag{2.35}$$

In [4] we used the constant penalty approach with a $[\![u]\!]_\perp^* = -W$, $P^* = 10$, where W is the interface thickness. Allowing a negative normal displacement jump was necessary to avoid numerical instabilities resulting from the use of a discontinuous penalty function, i.e. Eq. 2.35. Using a discontinuous interpenetration penalty function results in a discontinuous interface stiffness, which leads to a discontinuous algorithmic tangent. A discontinuous algorithmic tangent degrades the overall convergence rate of the finite element solver thus increasing the computational cost. In the worst case, the finite element solver might not even be able to converge at all. In general, convergence becomes more and more difficult as more interface elements are subject to compressive stress states. The reverse loading leg of a creep-fatigue simulation induces compressive stresses on many of the grain boundaries in a simulation volume. To avoid numerical issues while improving convergence we propose a quadratic penalty approach. The quadratic formulation was selected because it is the simplest polynomial function generating a C^1 continuous penalty formulation.

$$P = \begin{cases} 1 \quad \text{if} \quad [\![u]\!]_\perp \geq 0 \\ \\ a[\![u]\!]_\perp^2 + b[\![u]\!]_\perp + c \quad \text{if} \quad [\![u]\!]_\perp < 0 \end{cases} \tag{2.36}$$

The coefficients a, b, c of Eq. 2.36 have been formulated to enforce a penalty value of P^* at a normal displacement jump $[\![u]\!]_\perp = -W$, and to enforce C^1 continuity of the stiffness for $[\![u]\!]_\perp = -W$:

$$a = \frac{P|_{-W} - 1}{W^2} \tag{2.37}$$

$$b = 0 \tag{2.38}$$

$$c = 1 \tag{2.39}$$

where W is a parameter giving a critical interpenetration displacement and is independent from the real interface thickness. Proper calibration of the parameters $P|_{-W}$ and W prevents interpenetration while stabilizing the simulation numerics.

Figure 2.7 depicts the penalty P as function of the normalized displacement jump $[\![u]\!]_\perp$ for a discontinuous, linear and quadratic penalty function formulation.

Figures 2.8 and 2.9 depicts the change in the interpenetration penalty factor as function of the normalized displacement jump. In Figure 2.8, $P|_{-W}$ is fixed an W is changed. In Figure 2.9, W is fixed an $P|_{-W}$ is changed. Figures 2.9 shows the change in interpenetration penalty factor as a function of the selected $P|_{-W}$ value while keeping W fixed.

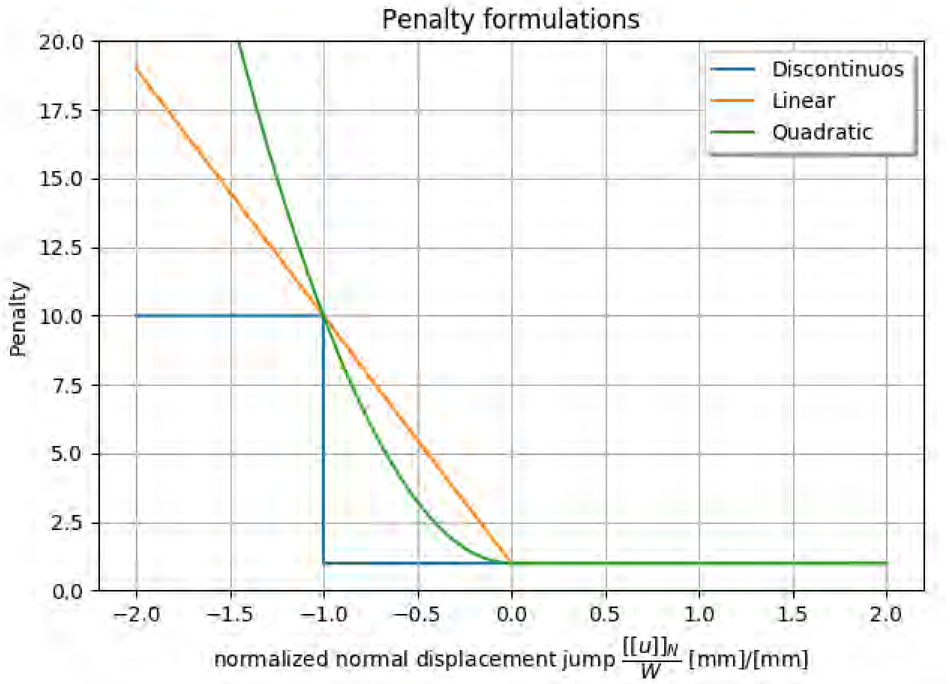

Figure 2.7: Inner-penetration penalty for different penalty models.

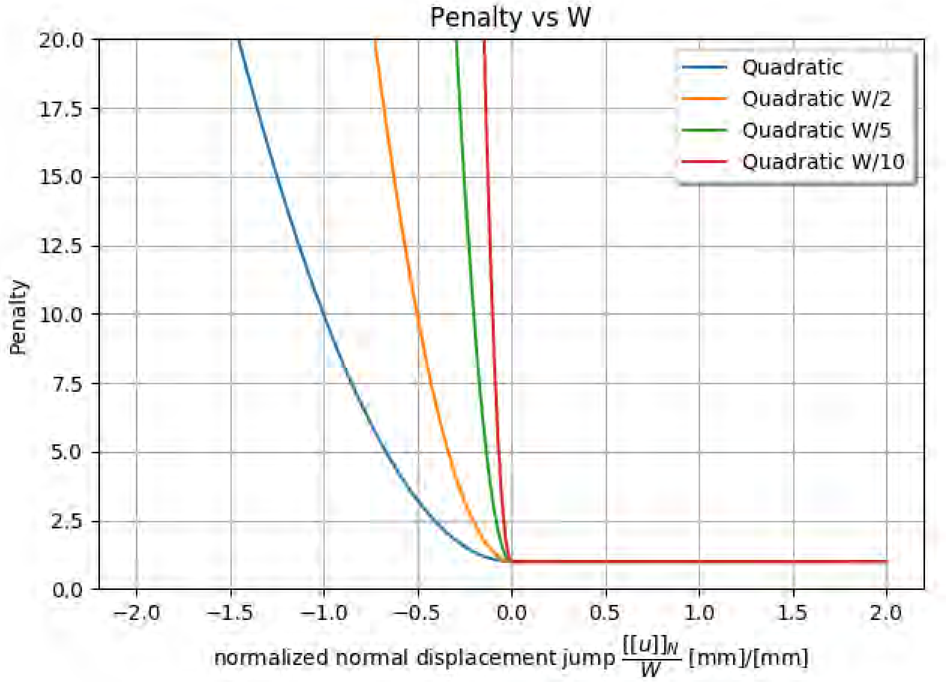

Figure 2.8: Change of the interpenetration penalty function as function of the interface thickness W

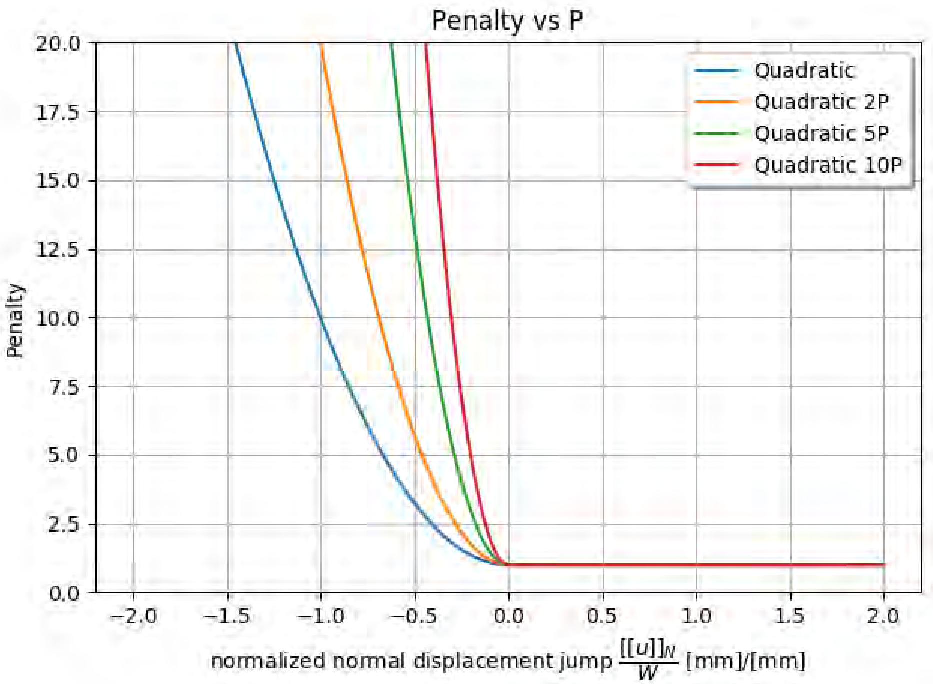

Figure 2.9: Change of the interpenetration penalty function as function of the penalty parameter P

2.4.2 Large deformation RVE strain decomposition

Nassif et al. [1] decomposes the total RVE strain, $\bar{\varepsilon}_{RVE}$ and strain rate, $\dot{\bar{\varepsilon}}_{RVE}$, into different deformation mechanisms. This methodology starts from the assumption that the average RVE strain is the sum of the average strain of the bulk material, $\bar{\varepsilon}_{GRAIN}$, and the strain introduced by the grain boundary deformation $\bar{\varepsilon}_{GB}$:

$$\bar{\varepsilon}_{RVE} = \frac{\int_V \varepsilon_{GRAIN} dV}{V_0} + \bar{\varepsilon}_{GB} \tag{2.40}$$

where V and V_0 are the deformed and undeformed volume of the grains. The first term of equation 2.40 represents the average strain in the grains. Computing the grain boundary strain is not trivial because cohesive interfaces do not have an initial geometrical thickness. To avoid this problem we can relate the grain boundary strain to the interface volume:

$$\bar{\varepsilon}_{GB} = \frac{\int_A T_{GB} dA}{V_0}. \tag{2.41}$$

where V_0 is volume of the grains in the undeformed configuration, A is the deformed grain boundary area, and T_{GB} is a tensorial quantity representing the contribution of the interface deformation to the volume change. Equation 2.41 does not properly account for large grain boundary area changes because the volume change is not related to the undeformed grain boundary area, A_0. Integrating 2.41 over A_0 would also produce inaccurate results as deformations will not be properly weighted. The proper scaling for Eq. 2.41 is the ratio between the undeformed and deformed grain boundary area:

$$\bar{\varepsilon}_{GB} = \frac{\int_A T_{GB} dA}{V_0} \frac{A_0}{A}. \tag{2.42}$$

The tensor T_{GB} is the symmetric part of the outer product between the grain boundary normal, n, and the interface displacement jump vector, $[\![u]\!]$:

$$T_{GB} = \frac{[\![u]\!] \otimes n^T + n \otimes [\![u]\!]^T}{2} \tag{2.43}$$

where the superscript T denotes the transpose. Both grain boundary opening and grain boundary sliding contribute to the total RVE average strain. The grain boundary opening contribution is

$$T_{GB\perp} = [\![u]\!] \cdot n \left(n \otimes n^T\right) = [\![u]\!]_\perp \left(n \otimes n^T\right) \tag{2.44}$$

and the grain boundary sliding contribution is:

$$T_{GB\parallel} = T_{GB} - T_{GB\perp} \tag{2.45}$$

Eventually, the interface opening and sliding strain contributions to the average RVE strain can be computed as follows:

$$\bar{\varepsilon}_{GB\perp} = \frac{\int_A T_{GB\perp} dA}{V_0} \frac{A_0}{A}. \tag{2.46}$$

$$\bar{\varepsilon}_{GB\parallel} = \frac{\int_A T_{GB\parallel} dA}{V_0} \frac{A_0}{A}. \tag{2.47}$$

Computing the total RVE strain rate requires either calculating the time derivatives of Eq. 2.40 or via numerical differentiation of the integrated quantities. While using rate equation is more rigorous, the current implementation relies on numerical differentiation because the rate quantities are not readily available. The implementation of the strain partitioning post-processing tool has been validated on a simple test case. The test case consists of an initially cubic domain with two grains linked by an elastic cohesive interface that is first stretched and then rotated. To allow large area changes, an elastic perfectly plastic material has been used to model the grain bulk response. The grain material is soft compared to the interface. Displacement is applied on the domain face parallel to the interface until the total domain strain in the loading direction is $\varepsilon_{zz} = 50\%$. The theoretical engineering strain of the domain is calculated as $\varepsilon_{zz} = \frac{1.5 l_0 - l_0}{l_0}$. The theoretical interface strain contribution is calculated as $\varepsilon_{zz,interface} = \frac{[\![u]\!]_\perp + l_0 - l_0}{l_0}$, where the value of $[\![u]\!]_\perp$ is extracted directly from the simulation. At simulation time $t = 1$ a 90° rigid body rotation is imposed around the y axis. Rigid body rotation is completed at time $t = 2$. Figure 2.12 depicts the domain at different simulation times. Theoretical results are compared against the strain partitioning algorithm. Figure 2.10 depicts the xx, yy and zz components of the total domain strain, interface strain, and grain strain, obtained from the strain partitioning algorithm. The computed interface, grain, and total domain strains agree with the theoretical values. Figure 2.10 also show that the partitioning algorithm is able to correctly rotate the strains under rigid body rotations. Figure 2.11 is similar to Figure 2.12 but depicts strain rates instead of strains.

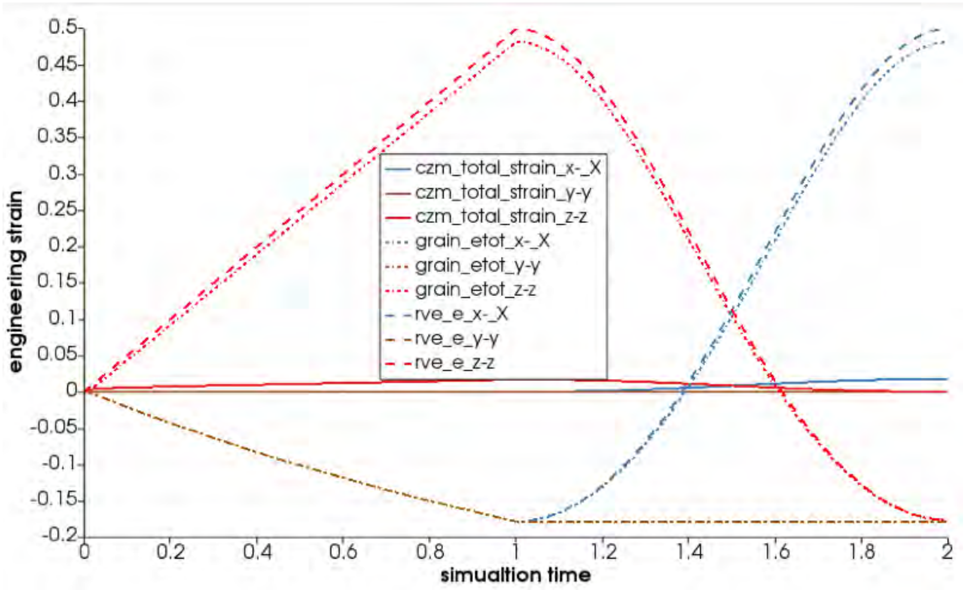

Figure 2.10: Engineering strain vs simulation time. Rigid body rotation starts at $t = 1$.

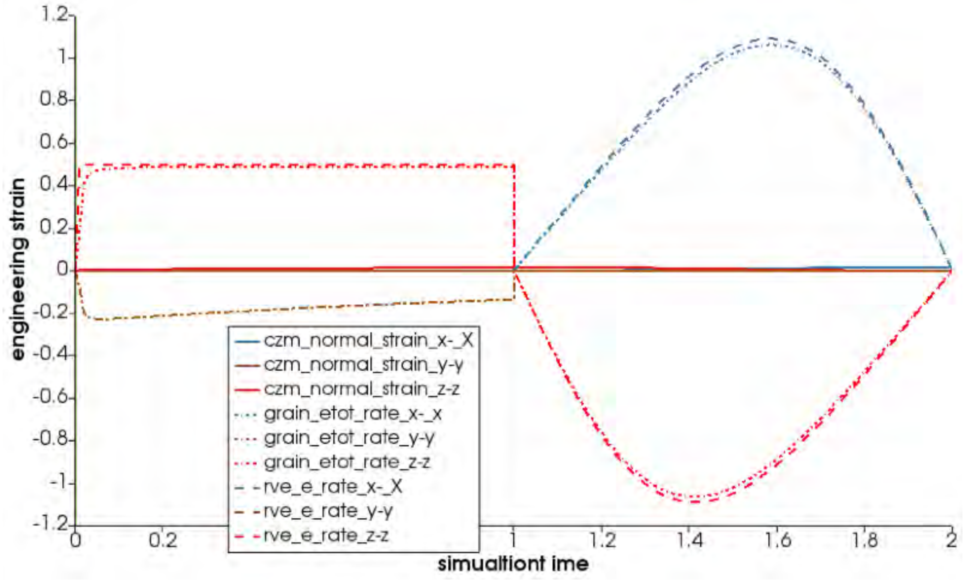

Figure 2.11: Engineering strain rate vs simulation time. Rigid body rotation starts at $t = 1$.

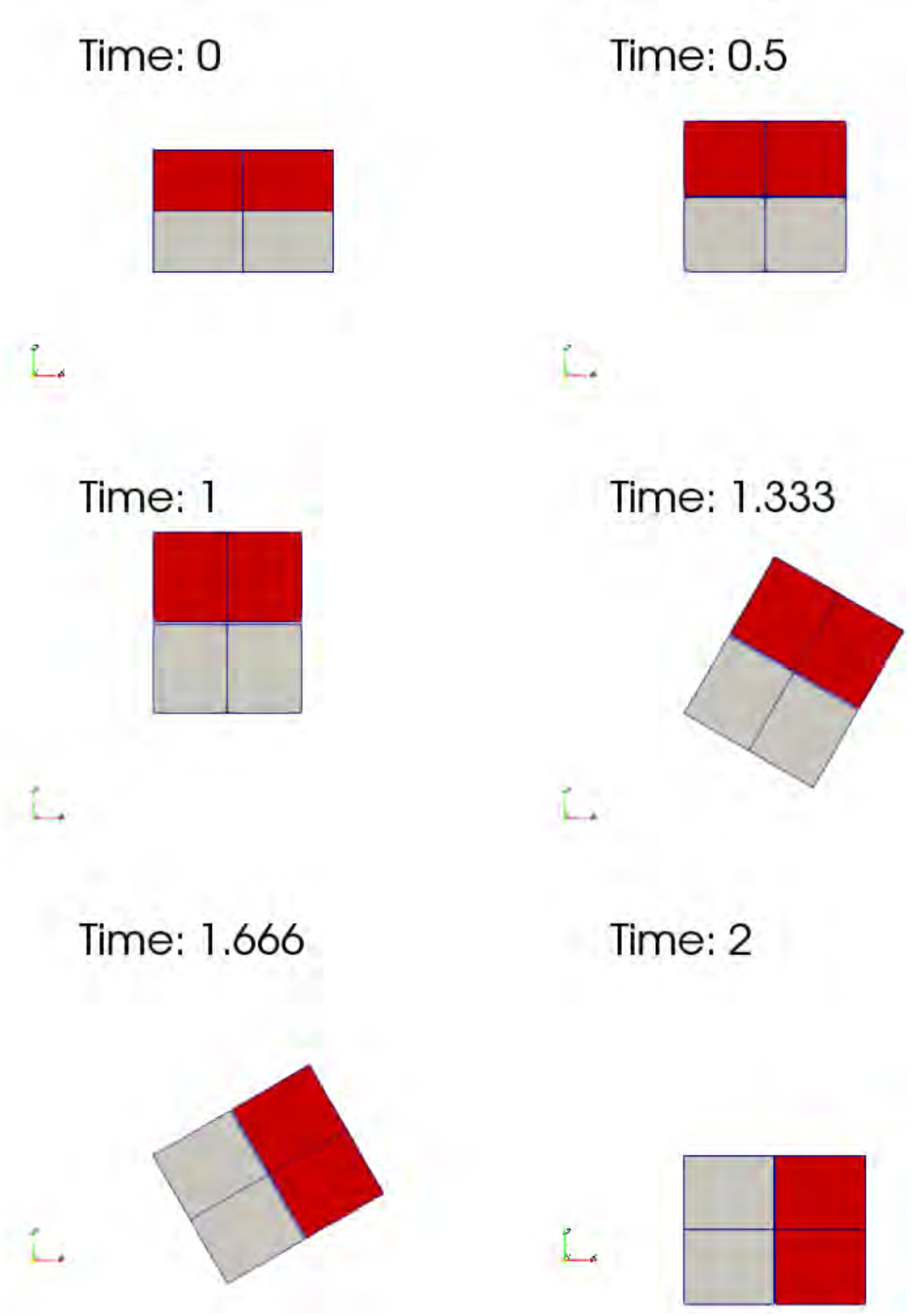

Figure 2.12: Graphical representation of the stretch plus rotation simulation used to validate the strain decomposition algorithm. Stretch is performed between time $t = 0$ and time $t = 1$. At time $t = 1$,$\varepsilon_z z = 50\%$. Rigid body rotation starts at time $t = 1$ and ends at time $t = 2$

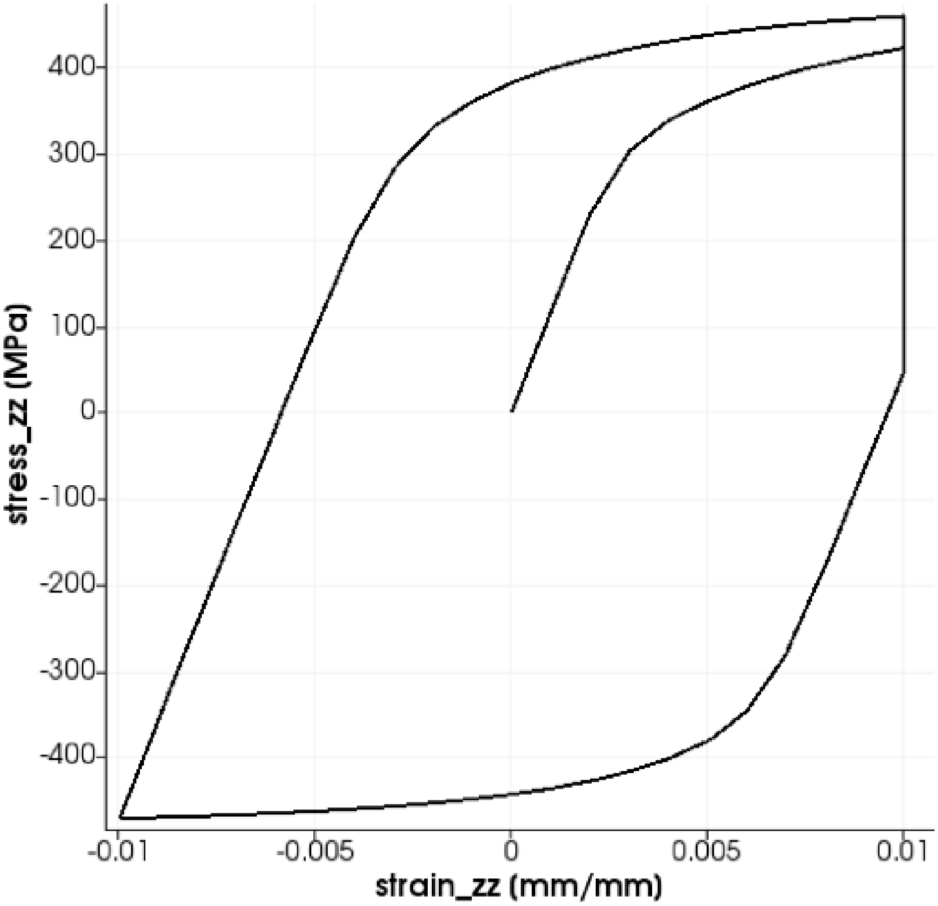

Figure 2.13: Plot of the RVE average stress versus RVE average strain for a creep fatigue simulation, including tensile hold.

2.4.3 Creep fatigue simulation results

This section presents results from a full creep-fatigue simulation. The test case used to validate the model is a creep fatigue cycle defined by a maximum strain in the loading direction of $\varepsilon_{max} = 1\%$, a hold time at maximum strain $H_{\varepsilon_{max}} = 1000\ h$, a minimum strain $\varepsilon_{min} = -1\%$, and no hold time at minimum strain. The strain rate used during transients is $10^{-4}\ {}^{1}/_{s}$, which is standard for creep-fatigue experiments. The results presented in this section include all the improvements made to the model, including large interface deformation, the augmented grain boundary cavitation model, the continuous interpenetration penalty model, and the soft contact model for failed grain boundaries. The RVE incorporates one-hundred randomly oriented grains. Figure 2.13 depicts the hysteresis loop of the first creep-fatigue cycle. Figure 2.13 also shows that the improved grain boundary cavitation model correctly captures the compressive portion of the creep-fatigue cycle including macroscopic kinematic and isotropic hardening.

Figure 2.14 depicts the average grain boundary and grain contribution to the total strain during hold. As expected, during the hold the elastic strain contribution drops while the inelastic strain increase and the interface strains increase to compensate.

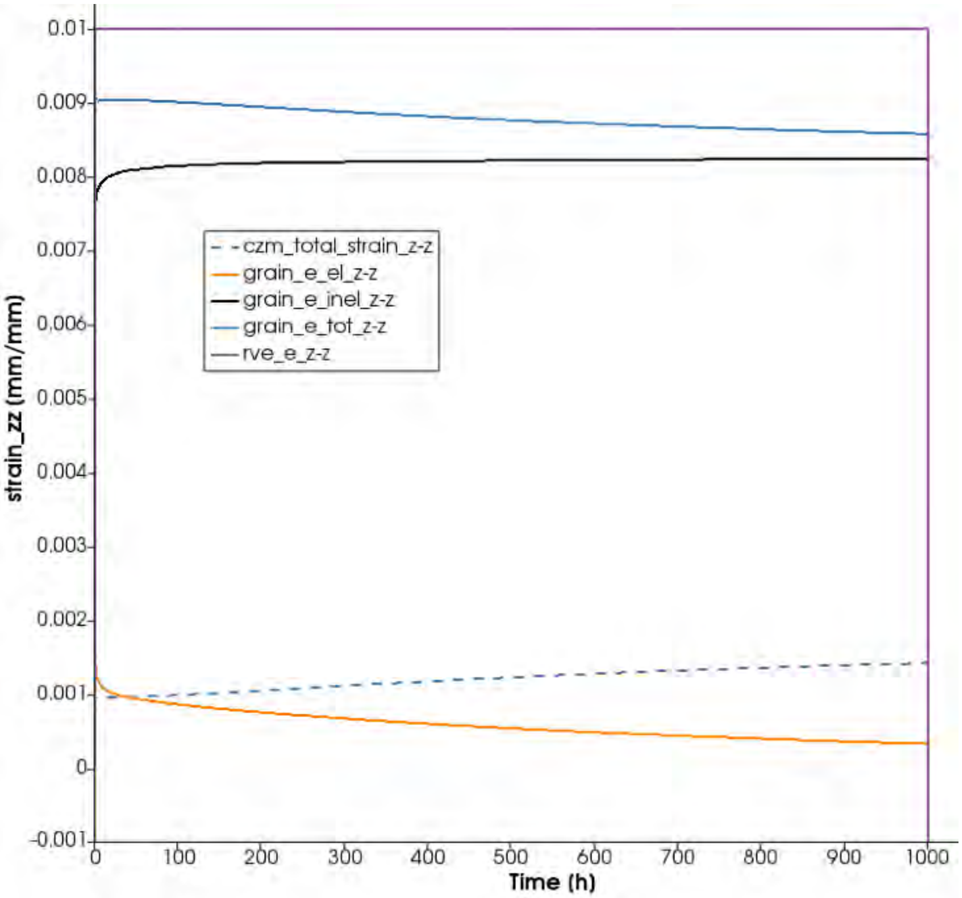

Figure 2.14: Plot of the RVE average stress versus time for a creep fatigue simulations, including tensile hold.

Figure 2.13 and 2.14 show that the strain partitioning algorithm is able to calculate the correct strains under large deformations. The total calculated RVE strain exactly matches the imposed strain.

3 Kinematic hardening

3.1 Background

As noted in Chapter 1, the current ANL crystal plasticity model does not include explicit kinematic hardening. On the macroscale, the model must represent kinematic hardening to accurately capture cyclic plasticity, which will be a key component of the complete creep-fatigue model [14].

Kinematic hardening models several key features of cyclic plasticity:

1. The Bauschinger effect [15] – on reverse loading the material yields at a lower absolute value of stress than the final flow stress on the forward loading branch.
2. Cyclic hardening and plastic shakedown – the material's cyclic hardening curve is different than its monotonic hardening curve. The cyclic hardening curve saturates at a different rate than the monotonic curve.
3. Ratcheting – under non-fully-reversed stress-controlled loading the material hysteresis loop moves in the tensile or compressive direction.
4. Mean stress relaxation – under non-fully-reversed strain-controlled loading the average stress during the cyclic deformation tends to move towards zero, i.e. a symmetric cycle.

All of these factors are important when modeling fatigue or creep-fatigue damage as they determine the stress/strain/time history experienced by the material.

Full field crystal plasticity models [16] or homogenized models capturing grain-to-grain interaction [17] naturally include a moderate kinematic hardening effect through the drag stress caused by neighboring grains preventing the free reinorientation of the material. The bulk crystal model from the original, monotonic creep model for Grade 91 can represent this type of kinematic hardening. Figure 3.1 is a full-field CPFEM model of simple cubic grains. The crystal model does not contain an explicit kinematic hardening term – essentially it has the same form as the ANL model for monotonic creep in Grade 91 [4]. The material has a random texture. The model undergoes a single load reversal, shown in the figure as an average, homogenized stress/strain curve for the polycrystal. This curve shows a Bauschinger effect – the initial, forward load flow stress is higher than the backward yield stress.

To some extent then kinematic hardening is an emergent property of a full-field crystal plasticity model – kinematic hardening emerges without an explicit kinematic hardening term in the slip system flow model. However, preliminary simulations at ANL indicated a need to include an explicit representation of kinematic hardening in the slip system strength models for two reasons:

1. The "natural" kinematic hardening cannot be controlled or tuned to match a particular material response. The only way to affect this emergent kinematic hardening is by changing the material texture or, to a lesser extent, grain morphology. A microstructural model for creep-fatigue requires better control of kinematic hardening to match the experimentally-observed, macroscale Grade 91 response.
2. The emergent kinematic hardening is too weak to cause all the cyclic plasticity effects observed in Grade 91 on the macroscale.

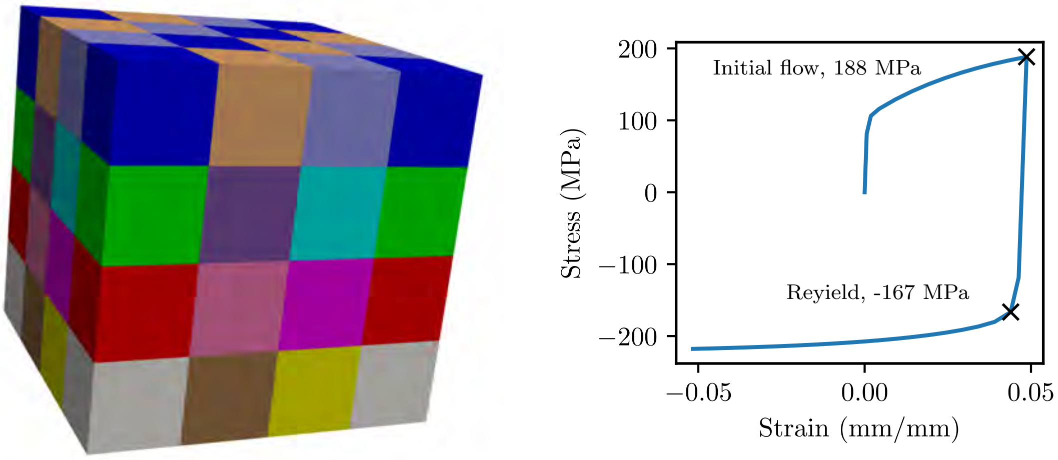

Figure 3.1: Example simulation demonstrating the Bauschinger effect occurs even for a crystal plasticity model without explicit kinematic hardening. The left subfigure shows the fully-resolved polycrystal: a 4 × 4 × 4× array of cubic grains. The right subfigure shows the volume-average stress/strain history for the cell loaded uniaxially. The final forward flow stress and the reyield stress are somewhat different.

Similarly, several authors have posited that non-local, gradient-based theories for the hardening effect of geometrically necessary dislocations (GNDs) can partly explain kinematic hardening (c.f. [18–20]). The authors explored this approach by implementing a simple gradient-based hardening theory in the NEML framework. These preliminary simulations had the same challenges as the emergent, texture-based kinematic hardening – the effect could not be easily tuned and was too weak to fully explain cyclic plasticity in Grade 91.

Therefore, we modified the ANL crystal plasticity framework to include explicit slip-system kinematic hardening.

3.2 Implementation

3.2.1 Monotonic model

The basic NEML crystal plasticity framework [4] is defined by the evolution equation for stress:

$$\dot{\boldsymbol{\sigma}} = \mathbf{C} : \left(\mathbf{d} - \mathbf{d}_p - \mathbf{S} : \sigma \cdot \boldsymbol{\Omega}^{\star} + \boldsymbol{\Omega}^{\star} \cdot \mathbf{S} : \sigma\right) \tag{3.1}$$

and the evolution equation for orientation:

$$\boldsymbol{\Omega}^{e} = \dot{\mathbf{R}}^{e}\mathbf{R}^{eT} = \mathbf{w} - \mathbf{w}_p - \boldsymbol{\varepsilon}\mathbf{d}_p + \mathbf{d}_p\boldsymbol{\varepsilon} \tag{3.2}$$

In these expressions

$$\boldsymbol{\Omega}^{\star} = \boldsymbol{\Omega}^{e} + \mathbf{w}_p \tag{3.3}$$

and $\mathbf{d}_p$ and $\mathbf{w}_p$ are the symmetric and skew parts, respectively, of

$$\mathbf{l}_p = \mathbf{R}^{e}\bar{\mathbf{l}}_p\mathbf{R}^{eT}. \tag{3.4}$$

with

$$\bar{\mathbf{l}}^p = \sum_{i=1}^{n_{slip}} \dot{\gamma}_i \left(\mathbf{Q}_0 \cdot \mathbf{d}_i \otimes \mathbf{n}_i \cdot \mathbf{Q}_0^T \right) \tag{3.5}$$

where $\mathbf{Q}_0$ is the initial grain orientation, $\mathbf{d}_i$ is the slip system direction, and $\mathbf{n}_i$ is the slip system normal. The slip rate model, $\dot{\gamma}_i$ contains all the model's constitutive assumptions — the kinematic details here are common to all NEML crystal models.

The *previous* crystal model in the ANL creep simulation framework for Grade 91 used the slip model:

$$\dot{\gamma}_i = \dot{\gamma}_i^{(0)} \frac{\tau_i}{\bar{\tau}_i} \left| \frac{\tau_i}{\bar{\tau}_i} \right|^{n-1} \tag{3.6}$$

with $\dot{\gamma}_0$ and n parameters and

$$\bar{\tau}_i = \hat{\tau}. \tag{3.7}$$

$$\dot{\bar{\tau}} = \delta \left(\tau_{sat} - \bar{\tau} \right) \sum \left| \dot{\gamma}_i \right| \tag{3.8}$$

With this constitutive model all the slip systems share the same slip system strength, which evolves with a standard Voce-type saturation equation. Ignoring grain-grain interactions, for example in a simple Taylor model, this formulation only produces isotropic hardening.

3.2.2 Cyclic model

Various models have been proposed for slip-system level kinematic hardening (c.f. [21–24]). The goal of the crystal plasticity model in the NEML framework is to be general, so that we can develop or adopt a model suitable for Grade 91 without substantial additional work in the future. Most of the literature models start with a slip system flow rule similar to:

$$\dot{\gamma}_i = \dot{\gamma}_0 \left\langle \frac{\left| \tau_i - \bar{\tau}_i^{back} \right| - \bar{\tau}_i^{iso}}{\bar{\tau}_i^{resistance}} \right\rangle^n \operatorname{sign}\left(\tau_i - \bar{\tau}_i^{back} \right). \tag{3.9}$$

In this model $\langle\rangle$ are the Macauly brackets and the strengths $\bar{\tau}_i^{iso}$, $\bar{\tau}_i^{back}$, and $\bar{\tau}_i^{reistance}$ are all strength models that can evolve based on an evolution equation, including an unlimited number of model internal variables, each with their own individual evolution equations.

This flexibility supports a wide variety of model types. Essentially, any model with a non-zero "backstrength" term ($\bar{\tau}_i^{back}$) will explicitly represent kinematic hardening effects. The following subsections detail the various hardening models available. Again, the hardening models can be used for any of the three generic strength terms in Eq. 3.9.

3.2.2.1 Models where all slip systems share the same strength

For these models

$$\bar{\tau}_i = \hat{\tau}. \tag{3.10}$$

meaning all slip systems share a single strength.

Linear hardening Simple linear hardening used mostly for testing:

$$\dot{\bar{\tau}} = k_1 \left| \dot{\gamma}_i \right| \tag{3.11}$$

Voce hardening This is the Voce model used in the original ANL framework for creep, implemented in the new modeling framework:

$$\dot{\bar{\tau}} = \delta \left(\tau_{sat} - \bar{\tau}\right) \sum \left|\dot{\gamma}_i\right| \tag{3.12}$$

3.2.2.2 Models where each slip system has its own strength

Fixed strength hardening All slip system have a unique value of slip system strength but all the values are constants:

$$\bar{\tau}_i = c_i \tag{3.13}$$

Generalized linear hardening This model implements a general linear model where the slip system strength evolves with one of two similar evolution equations, either:

$$\dot{\bar{\tau}}_i = \sum_{j=1}^{n_{total}} M_{kj} \dot{\gamma}_j \tag{3.14}$$

or

$$\dot{\bar{\tau}}_i = \sum_{j=1}^{n_{total}} M_{kj} \left|\dot{\gamma}_j\right| \tag{3.15}$$

The first form is suitable for back strength models, as the strength can be either positive or negative. The second form is suitable for isotropic hardening models or drag stress models, where the strength should not become negative.

Slip system Voce hardening This model is similar to the single-strength Voce model except each system has its own hardening variable:

$$\dot{\bar{\tau}}_i = k_i \left(1 - \frac{\bar{\tau}_i - \tau_i^{(0)}}{\tau_i^{(sat)} - \tau_i^{(0)}}\right)^{m_i} \left|\dot{\gamma}_i\right| \tag{3.16}$$

Slip system Frederick-Armstrong hardening This model, originally presented in [25], is the microscale equivalent of the classical Frederick-Armstrong [26] model:

$$\dot{\bar{\tau}}_i = c_i \left(\dot{\gamma}_i - \frac{\bar{\tau}_i}{\tau_i^{(final)}} \left|\dot{\gamma}_i\right|\right) \tag{3.17}$$

3.3 Verification and examples

The framework implemented in the NEML crystal plasticity model covers a vast array of potential models for microscale kinematic hardening. Future work will develop a model specifically for Grade 91 at the temperatures of interest and calibrate it to data.

This section provides verifications examples using a basic form of the general modeling framework:

Parameter	Description	Value	Units
E	Young's modulus	160000	MPa
ν	Poisson's ratio	0.31	-
$\dot{\gamma}_0$	Reference slip rate	10^{-4}	1/s
n	Rate sensitivity	10	-
k	Isotropic initial slope	3200	MPa
$\tau^{(0)}$	Isotropic initial value	50	MPa
$\tau^{(sat)}$	Isotropic saturation	100	MPa
m	Isotropic Voce exponent	1	-
c	Kinematic initial slope	800	MPa
$\tau^{(final)}$	Kinematic saturation	150	MPa

Table 3.1: Model parameters for the verification simulations.

- $\bar{\tau}_i^{iso}$: slip system Voce hardening
- $\bar{\tau}_i^{reistance}$: fixed strength
- $\bar{\tau}_i^{back}$: slip system Frederick-Armstrong hardening

This model is the microstructural equivalent of the classical Frederick-Armstrong model superimposed with Voce isotropic hardening. Table 3.1 lists the parameters for the verification simulations. All these simulations are for a Taylor-homogenized polycrystal with 100 random orientations. This model does not include grain-to-grain interactions and so the kinematic hardening effect arises entirely from the slip system model.

3.3.1 Bauschinger effect

Figure 3.2 demonstrates the new crystal plasticity model represents the Bauschinger effect. This simulation is a single cycle under fully-reversed strain controlled loading. The yield stress on the first reversal is lower (in absolute value) than the flow stress at the end of the loading leg.

3.3.2 Cyclic hardening

Figure 3.3 plots three overlapping stress/time histories. The first is from a fully-reversed, strain-controlled simulation. The other two histories are from monontic simulations covering the same total time/strain as the cyclic test. One simulation applies tensile load, the other compressive.

The key result is that the monotonic hardening curves and the cyclic hardening curve (the locus of points at either the extreme tension or extreme compression values of each cycle) are different. This is another manifestation of kinematic hardening. The new crystal model can independently tune the isotropic and kinematic hardening to match macroscale experimental data.

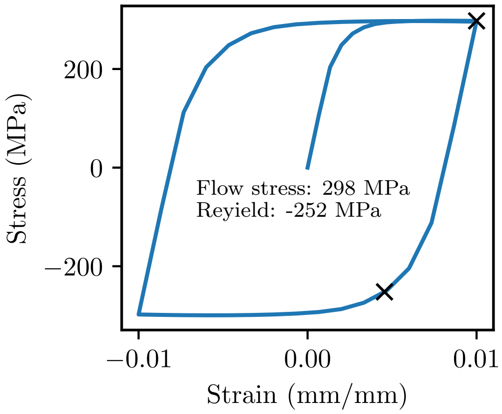

Figure 3.2: Demonstration of the Bauschinger effect in the new crystal model.

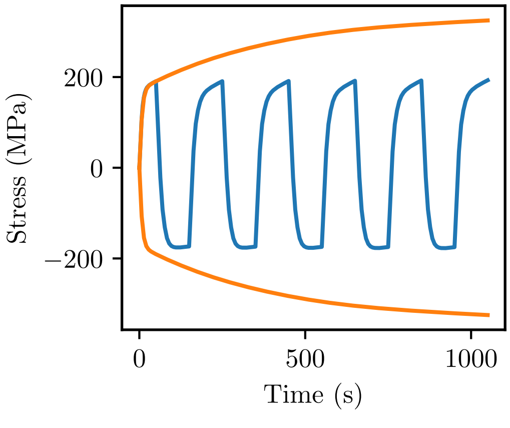

Figure 3.3: Demonstration that the cyclic and monotonic hardening curves are different in the new crystal model and that the material flow stress saturates at different rates in monotonic and cyclic tests.

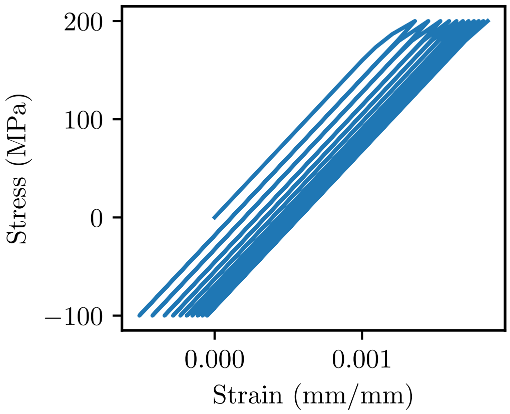

Figure 3.4: The new crystal model demonstrates ratcheting and shakedown behavior in stress-controlled simulations.

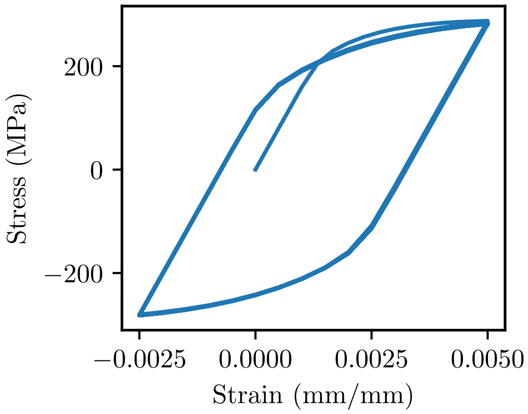

Figure 3.5: The mean stress rapidly relaxes out in strain controlled cyclic simulations for these crystal model parameters.

3.3.3 Ratcheting

Figure 3.4 shows the model results for non-fully-reversed stress-controlled loading. The model exhibits ratcheting and shakedown behavior – at first the hysteresis loop marches towards the tensile direction but over time this ratcheting abates and the loop stabilizes. Again, this is a manifestation of kinematic hardening and the new crystal model can tune the stress-controlled material ratcheting to match experimental data.

3.3.4 Mean stress relaxation

Finally, Figure 3.5 demonstrates the crystal model represents mean stress relaxation. Under non-fully-reversed strain control loading the initial slight bias towards a tensile mean stress relaxes away – rapidly, for this particular parameter set.

3.3.5 Summary

These example simulations verify the new crystal model can capture all the cyclic plasticity effects required to accurately represent the bulk, undamaged response of Grade 91. The primary remaining work on this topic is to recalibrate the Grade 91 model using the new kinematic hardening options to capture the experimentally-observed response of Grade 91. The undamaged portion of macroscale strain-controlled (creep-fatigue) and stress-controlled (ratcheting) cyclic experiments can be used to calibrate the model. Taylor homogenization will be used in this initial calibration to avoid the computational expense of full-field models. Likely some adjustment to this initial parameter set will be required, as the introduction to this chapter demonstrates that full-field simulations include an additional kinematic hardening effect solely through grain-to-grain interactions.

4 Conclusions and future work

This report describes a preliminary microstructural model for creep-fatigue in Grade 91 steel. The current model accurately represents undamaged cyclic plasticity and grain boundary cavitation in a CPFEM framework. This required substantial improvements to both the bulk crystal plasticity formulation NEML and to the grain boundary interface damage model in MOOSE. The current model can represent cyclic plasticity with cavitation damage on grain boundaries (see Figure 2.13) but cannot yet model transgranular fatigue cracking. Additional work, not described in detail here, concerned the development of a geometric hardening model in the combined NEML/MOOSE CPFEM framework and scoping studies on the emergent kinematic hardening in full-field mesoscale simulations of representative polycrystals. As described in Chapter 3, these effects are not sufficient to fully represent the kinematic hardening in Grade 91 on the macroscale. However, the capabilities were merged into MOOSE and NEML and could be used in future modeling efforts.

The main remaining development task in completing a model for creep-fatigue interaction is including a fatigue damage modeling mechanism in the CPFEM framework. We have begun developing such a model based on a continuum damage formulation in the NEML crystal model. This model will represent the degradation in elastic stiffness in persistent slip bands, leading to the eventual development of a fatigue microcrack, represented with a smeared crack formulation.

The model will modify the crystal plasticity stress update equation (Eq. 3.1) to include *planar* continuum damage operating on multiple planes, similar to [27]:

$$\dot{\boldsymbol{\sigma}} = \left(\mathbf{I} - \sum_{j=1}^{n_{planes}} D_j \mathbf{P}_j\right) \mathbf{C} : \left(\mathbf{d} - \mathbf{d}_p - \mathbf{S} : \sigma \cdot \boldsymbol{\Omega}^{\star} + \boldsymbol{\Omega}^{\star} \cdot \mathbf{S} : \sigma\right) \tag{4.1}$$

where $\mathbf{P}_j$ is a projection operator, defined in [27], projecting damage onto a particular plane with normal vector $\mathbf{n}_j$ and D_j is a continuum damage variable ranging from 0 (undamaged) to 1 (no load carrying capability).

In the context of the crystal model, the index j will be over slip planes. All slip systems on a given plane defined by $\mathbf{n}_j$ will contribute to damage normal to that plane. The damage variable will evolve proportionally to some fatigue indicating parameter (FIP). Currently, we plan to use either:

$$D_j \sim \sum_{i=1}^{n^j_{slip}} \left|\dot{\gamma}_i\right| \tag{4.2}$$

where the sum occurs over all slip systems sharing slip plane j or, similarly,

$$D_j \sim \sum_{i=1}^{n^j_{slip}} \tau_i \dot{\gamma}_i. \tag{4.3}$$

The first model evolves fatigue damage proportional to the accumulated slip on the entire slip plane. The second model evolves damage proportional to the dissipated work, again on that particular plane. These basic proportionality equations will need to be altered to better match the physical response of the material, e.g. damage should not accumulate linearly, and to improve the model numerics, e.g. the damage model should decay gracefully to zero load carrying capacity.

With this final model feature implemented the CPFEM model could be recalibrated now to capture the available creep-fatigue data, as opposed to the creep data captured by the previous incarnation. Once validated, this framework will be used to assess:

1. Creep-fatigue damage in material loaded with realistic *component* loading conditions. Actual components typically experience much smaller strain ranges and primary loads and much longer hold times than accelerated creep-fatigue tests.
2. Simulations of multiaxial creep-fatigue to validate and/or improve the ASME approach to multiaxial creep-fatigue design

Both of these issues are critical in designing efficient core block microreactor components. In addition, the model will be a framework for better-understanding the microstructural origins of creep-fatigue, which could lead to radically improved design methods and structural materials.

Acknowledgements

The research was sponsored by the U.S. Department of Energy, under Contract No. DEAC02-06CH11357 with Argonne National Laboratory, managed and operated by UChicago Argonne LLC. Programmatic direction was provided by the Office of Nuclear Reactor Deployment of the Office of Nuclear Energy. The authors gratefully acknowledge the support provided by Sue Lesica, Federal Manager, Advanced Materials, Advanced Reactor Technologies (ART) Program, Tom Sowinski, Federal Manager, Microreactor Program, and Jess C. Gehin of Idaho National Laboratory, National Technical Director, Microreactor Program.

Bibliography

[1] Omar Nassif, Timothy Truster, Ran Ma, Kristine Cochran, David Parks, Mark Christian Messner, and T-L Sham. Combined crystal plasticity and grain boundary modeling of creep in ferritic-martensitic steels, part 1: Theory and implementation. *Modelling and Simulation in Materials Science and Engineering*, 2019.

[2] Mark Christian Messner, Omar Nassif, Ran Ma, Timothy Truster, Kristine Cochran, David Parks, and T-L Sham. Combined crystal plasticity and grain boundary modeling of creep in ferritic-martensitic steels, part 2: The effect of stress and temperature on engineering and microstructural properties. *Modelling and Simulation in Materials Science and Engineering*, 2019.

[3] MC Messner, A Rovinelli, DM Parks, and T-L Sham. Evaluation of statistical variation of microstructural properties and temperature effects on creep fracture of grade 91. Technical report, Argonne National Lab.(ANL), Argonne, IL (United States), 2018.

[4] A. Rovinelli, M. C. Messner, Guosheng Ye, and T.-L. Sham. Initial study of notch sensitivity of grade 91 using mechanisms motivated crystal plasticity finite element method. Technical Report ANL-ART-171, Argonne National Laboratory, Lemont, IL, USA, 2019.

[5] M. C. Messner, R. I. Jetter, and T.-L Sham. A High Temperature Primary Load Design Method Based on Elastic Perfectly-Plastic and Simplified Inelastic Analysis. In *Proceedings of the ASME 2020 Pressure Vessels and Piping Conference*, pages PVP2020–21470, 2020.

[6] Soo Woo Nam, Soo Chan Lee, and Je Min Lee. The effect of creep cavitation on the fatigue life under creep-fatigue interaction. *Nuclear Engineering and Design*, 153(2-3): 213–221, 1995. ISSN 00295493. doi: 10.1016/0029-5493(95)90013-6.

[7] John Wareing. Creep-fatigue interaction in austenitic stainless steels. *Metallurgical Transactions A*, 8(5):711–721, 1977. ISSN 03602133. doi: 10.1007/BF02664781.

[8] B. Fournier, M. Salvi, F. Dalle, Y. De Carlan, C. Caës, M. Sauzay, and A. Pineau. Lifetime prediction of 9-12%Cr martensitic steels subjected to creep-fatigue at high temperature. *International Journal of Fatigue*, 32(6): 971–978, 2010. ISSN 01421123. doi: 10.1016/j.ijfatigue.2009.10.017. URL `http://dx.doi.org/10.1016/j.ijfatigue.2009.10.017`.

[9] P. Rodriguez and K. Bhanu Sankara Rao. Nucleation and growth of cracks and cavities under creep-fatigue interaction. *Progress in Materials Science*, 37(5):403–480, 1993. ISSN 00796425. doi: 10.1016/0079-6425(93)90006-7.

[10] M. Sauzay, M. Mottot, L. Allais, M. Noblecourt, I. Monnet, and J. Périnet. Creep-fatigue behaviour of an AISI stainless steel at 550 C. *Nuclear Engineering and Design*, 232(3):219–236, 2004. ISSN 00295493. doi: 10.1016/j.nucengdes.2004.05.005.

[11] Dong Feng Li, Richard A. Barrett, Padraic E. O'Donoghue, Noel P. O'Dowd, and Sean B. Leen. A multi-scale crystal plasticity model for cyclic plasticity and low-cycle fatigue in a precipitate-strengthened steel at elevated temperature. *Journal of the Mechanics and Physics of Solids*, 101:44–62, 2017. ISSN 00225096. doi: 10.1016/j.jmps.2016.12.010.

[12] Nailong Zhao, Anish Roy, Weizhe Wang, Liguo Zhao, and Vadim V. Silberschmidt. Coupling crystal plasticity and continuum damage mechanics for creep assessment in Cr-based power-plant steel. *Mechanics of Materials*, 130(December 2018):29–38, 2019. ISSN 01676636. doi: 10.1016/j.mechmat.2019.01.006. URL `https://doi.org/10.1016/j.mechmat.2019.01.006`.

[13] Agusti Perez-Foguet, Antonio Rodriguez-Ferran, and Antonio Huerta. Consistent tangent matrices for substepping schemes. *Computer methods in applied mechanics and engineering*, 190(35-36):4627–4647, 2001.

[14] J. L. Chaboche. A review of some plasticity and viscoplasticity constitutive theories. *International Journal of Plasticity*, 24(10):1642–1693, oct 2008. ISSN 07496419. doi: 10.1016/j.ijplas.2008.03.009. URL `http://linkinghub.elsevier.com/retrieve/pii/S0749641908000582`.

[15] P. S. Bate and D. V. Wilson. Analysis of the bauschinger effect. *Acta Metallurgica*, 34 (6):1097–1105, 1986. ISSN 00016160. doi: 10.1016/0001-6160(86)90220-8.

[16] Markian P. Petkov, Jianan Hu, Edmund Tarleton, and Alan C.F. Cocks. Comparison of self-consistent and crystal plasticity FE approaches for modelling the high-temperature deformation of 316H austenitic stainless steel. *International Journal of Solids and Structures*, 171:54–80, 2019. ISSN 00207683. doi: 10.1016/j.ijsolstr.2019.05.006.

[17] Youngung Jeong, Frédéric Barlat, and Myoung Gyu Lee. Crystal plasticity predictions of forward-reverse simple shear flow stress. *Materials Science Forum*, 702-703:204–207, 2012. ISSN 16629752. doi: 10.4028/www.scientific.net/MSF.702-703.204.

[18] C. J. Bayley, W. A M Brekelmans, and M. G D Geers. A comparison of dislocation induced back stress formulations in strain gradient crystal plasticity. *International Journal of Solids and Structures*, 43(24):7268–7286, 2006. ISSN 00207683. doi: 10.1016/j.ijsolstr.2006.05.011.

[19] L. P. Evers, W. A.M. Brekelmans, and M. G.D. Geers. Non-local crystal plasticity model with intrinsic SSD and GND effects. *Journal of the Mechanics and Physics of Solids*, 52(10):2379–2401, 2004. ISSN 00225096. doi: 10.1016/j.jmps.2004.03.007.

[20] Jobie M. Gerken and Paul R. Dawson. A crystal plasticity model that incorporates stresses and strains due to slip gradients. *Journal of the Mechanics and Physics of Solids*, 56(4):1651–1672, 2008. ISSN 00225096. doi: 10.1016/j.jmps.2007.07.012.

[21] Chung Souk Han, R. H. Wagoner, and Frédéric Barlat. On precipitate induced hardening in crystal plasticity: Theory. *International Journal of Plasticity*, 20(3):477–494, 2004. ISSN 07496419. doi: 10.1016/S0749-6419(03)00098-6.

[22] Conor Hennessey, Gustavo M. Castelluccio, and David L. McDowell. Sensitivity of polycrystal plasticity to slip system kinematic hardening laws for Al 7075-T6. *Materials Science and Engineering A*, 687(January):241–248, 2017. ISSN 09215093. doi: 10.1016/j.msea.2017.01.070. URL `http://dx.doi.org/10.1016/j.msea.2017.01.070`.

[23] T. Dick and G. Cailletaud. Fretting modelling with a crystal plasticity model of Ti6Al4V. *Computational Materials Science*, 38(1):113–125, 2006. ISSN 09270256. doi: 10.1016/j.commatsci.2006.01.015.

[24] Adnan Eghtesad and Marko Knezevic. High-performance full-field crystal plasticity with dislocation-based hardening and slip system back-stress laws: Application to modeling deformation of dual-phase steels. *Journal of the Mechanics and Physics of Solids*, 134, 2020. ISSN 00225096. doi: 10.1016/j.jmps.2019.103750.

[25] L. Méric and G. Cailletaud. Single crystal modeling for structural calculations: Part 2-finite element implementation. *Journal of Engineering Materials and Technology, Transactions of the ASME*, 113(1):171–182, 1991. ISSN 15288889. doi: 10.1115/1.2903375.

[26] C. O. Frederick and P. J. Armstrong. A mathematical representation of the multiaxial Bauschinger effect. *Materials at High Temperatures*, 24(1):1–26, 2007.

[27] M. C. Messner, A. J. Beaudoin, and R. H. Dodds. A grain boundary damage model for delamination. *Computational Mechanics*, 56(1):153–172, 2015. ISSN 0178-7675. doi: 10.1007/s00466-015-1164-z. URL `http://link.springer.com/10.1007/s00466-015-1164-z`.

Applied Materials Division
Argonne National Laboratory
9700 South Cass Avenue, Bldg. 212
Argonne, IL 60439

www.anl.gov

Argonne National Laboratory is a U.S. Department of Energy
laboratory managed by UChicago Argonne, LLC